Colloid Polym Sci 277:856–867 (1999)

ORIGINAL CONTRIBUTION

S. Haas
H. Hoffmann
C. Thunig
E. Hoinkis

Phase and aggregation behaviour of double-chain cationic surfactants from the class of *N*-alkyl-*N*-alkyl′-*N*,*N*-dimethylammonium bromide surfactants

Received: 7 April 1999
Accepted in revised form: 30 April 1999

S. Haas · H. Hoffmann (✉) · C. Thunig
University of Bayreuth
Physical Chemistry I
Universitätsstrasse 30
D-95447 Bayreuth
Germany

E. Hoinkis
Hahn-Meitner Institute
Glienicker Straße 100
D-14109 Berlin, Germany

Abstract We present the phase diagrams and the properties of newly synthesised double-chain cationic *N*-alkyl-*N*-alkyl′-*N*,*N*-dimethylammonium bromide surfactants [C_xC_yDMABr (x = 12, 14 and 16; y = 10, 11, 12, 14 and 16)]. All the systems studied form liquid-crystalline lamellar phases but with different morphologies: unilamellar vesicles at low surfactant concentrations, multilamellar vesicles and tubular aggregates for surfactant concentrations between 2 and 10 wt% and at even higher concentrations planar bilayers of surfactant molecules in the classical L_α phase. The phase diagrams were determined with macroscopic and microscopic methods (polarisation microscopy, freeze-fracture transmission electron microscopy, scanning electron microscopy and differential interference contrast microscopy). The properties of the surfactant solutions were determined with differential scanning calorimetry measurements for Krafft point determination and small-angle neutron scattering measurements for interlamellar spacing and bilayer thickness. Finally, conductivity and viscosity measurements for phase characterisation were carried out.

Key words Double chain surfactants · Aggregates · Phase diagrams · Lamellar phases · Electron microscopy · SANS

Introduction

The phase behaviour of surfactants in water is strongly influenced by their constitution as well as by external factors such as temperature, pressure or additives, for example, cosurfactants and salt [1–10]. The type of micelles (i.e. spheres, rods or discs) formed by surfactants in solution can be predicted by the packing parameter p defined by Israelachvili et al. [11] as the ratio of the volume of the hydrocarbon chain of the surfactant (v) and the product of the length of the alkyl chain (l) and the head group area per surfactant molecule (a_0):

$$p = \frac{v}{la_0} \quad .$$

Surfactants with p below 1/3 prefer the formation of spherical micelles, while p values between 1/3 and 1/2 favour the formation of rodlike micelles and p values greater than 1/2 favour the formation of disclike micelles. Surfactants with even higher values of p ($p > 1$) prefer the formation of lamellar aggregates or reverse micelles as the first stable aggregation form. Because the micellar shape determines the liquid-crystalline phases that are formed by the surfactants for high concentrations, the packing parameter is a very important factor to predict the phase behaviour of surfactants. By changing the packing parameter of a surfactant, for example, by adding short-chain alcohols as cosurfactants which strongly influence the head group area per molecule but do not change the volume of the hydrocarbon chain, the phase behaviour of the surfactants can be varied [12–16]. Instead of additives such as alcohols or salt the variation of alkyl chain lengths in double-chain surfactants is an easy way to control the phase behaviour of surfactants with respect to the volume and

the length of the hydrocarbon chains, while the head group area stays more or less the same for all surfactants. For the homologues of the double-chain cationic surfactants of the *N*-alkyl-*N*-alkyl′-*N*,*N*-dimethylammonium bromide-type (C_xC_yDMABr) Hertel and Hoffmann [17–19] found a strong dependence of the phase behaviour on the length of the alkyl chains x and y: while for the surfactants $C_{16}C_1$DMABr–$C_{16}C_4$DMABr an isotropic–nematic–hexagonal phase sequence was found, $C_{16}C_5$DMABr formed a hexagonal liquid crystalline phase after the micellar phase and for high concentrations a cubic phase. The two surfactants $C_{16}C_6$DMABr and $C_{16}C_7$DMABr did not form a liquid-crystalline phase for concentrations up to 80 wt%, while for $C_{16}C_8$DMABr the micellar region is followed by a L_1/L_α two-phase region and an inverse hexagonal phase for high surfactant concentrations. The same observations have been made for the homologous $C_{14}C_y$-DMABr. Based on these results this paper deals with the chain-length-dependent phase behaviour of the homologues of C_xC_yDMABr with even longer chains ($y > 8$). It is expected that these surfactants will just form lamellar liquid-crystalline phases, as was observed for $C_{12}C_{12}$DMACl, $C_{16}C_{16}$DMACl and $C_{18}C_{18}$DMACl by Kunieda and Shinoda [20] and for $C_{12}C_{12}$DMABr by Dubois and coworkers [21–23], with a great variety in aggregation form (unilamellar vesicles, planar bilayers).

Experimental

Materials

The surfactants investigated were synthesised in our laboratories by a quaternisation reaction of the *N*-alkyl-*N*,*N*-dimethylamine with a corresponding alkylbromide in acetonitrile. The two-phase reaction solution – the alkylbromide is soluble in acetonitrile, while the *N*-alkyl-*N*,*N*-dimethylamine is not soluble – is heated under reflux until a slightly yellow one-phase solution is obtained (20 min–4 h, depending on the length of the reactants). After cooling to room temperature, the solvent is removed in the vacuum and the corresponding raw product is obtained.

$$C_xDMA + C_yBr \xrightarrow{CH_3CN,80\,^\circ C} C_xC_yDMABr \ .$$

Dodecyl-, tetradecyl- and hexadecylamine were a gift from Hoechst-Gendorf with a purity of about 90–95%. The impurities were homologous amines with ± 2 CH_2 groups. The *n*-alkylbromides (y = 10, 11, 12, 14, 16) were supplied by Fluka (p.a. quality) and the solvent was from Merck (p.a. quality).

For further purification the raw product was recrystallised twice in a mixture of diethylether and methanol. The yield of the reaction was about 90%. Melting-point measurements for the characterisation of the final product could not be carried out because the quaternary ammonium salts decompose before melting. The purity of the surfactants can be seen from the surface tension measurements [24] which do not show any minima at the critical micelle concentration (cmc).

Phase diagrams

The samples for the phase diagrams were prepared by weight in double distilled water and kept in sealed tubes in a thermostated water bath. The samples were homogenised by heating and rigorous stirring. The temperature of the samples was varied between 15 and 70 °C. After increasing the temperature the samples were left for at least a week before the phase formed by the surfactants in water was determined. The liquid-crystalline phases formed by the surfactants were determined by the macroscopic textures of the samples between crossed polarisers using various microscopic techniques. Besides the liquid-crystalline texture, turbidity and other macroscopic properties such as viscosity and phase boundaries were used to characterise the samples.

Polarisation microscopy

For the determination of the liquid-crystalline structures formed in the surfactant solutions a Pol 16 polarisation microscope (Zeiss) was used. The samples were prepared in microslides of defined thickness. The birefringence texture is typical for certain kinds of liquid-crystalline phases; the use of a λ-plate allows the determination of the sign of the birefringence.

Differential interference contrast microscopy

Differential interference contrast microscopy (DICM) is a special type of light microscopy which allows details to be made visible which cannot be seen by common light microscopy because of the lack of contrast between the object and its surroundings. In a DIC microscope the light is first polarised and then divided by a Wollaston prism into two partial beams which are laterally displaced by a small distance and which have perpendicular polarisation planes. The anisotropy of the object causes a phase shift between the two partial beams because of the difference in their refractive indices. After passing the sample, the two partial beams are reunited by a second Wollaston prism and can interfere. By the use of an analyser perpendicular to the polariser the following picture can be seen: for a phase shift to $n\,\lambda$ (n = 0, 1, 2, …) between the two partial beams the image is dark and for all other phase shifts the brightness of the image corresponds to the different refractive indices of the molecules of the object. Therefore the images obtained by DICM appear very plastic. For our investigations we used an Axiovert 135 DIC microscope (Zeiss); the samples were prepared in microslides of defined thickness.

Scanning electron microscopy

The scanning electron microscopy (SEM) images were taken with a SEM 840-A microscope (Joel). The electrons are supplied from a heated tungsten wire and are accelerated with 100 kV. The sample is then scanned with this electron beam. The sample emits electrons which produce photons in a scintillator and induce a flow of electrons in the photocathode. The more the surface of the sample is inclined to the primary electron beam, the more electrons are emitted by the sample (relief contrast). The samples for SEM are prepared by the freezing-fracture (FF) technique. Thin layers are quickly quenched to low temperatures to prevent the formation of ice crystals. After the breaking of the sample, the water on the surface is removed by sublimation at 190 K. To get a good contrast, the sample is sputtered with a 10–20-nm-thick gold layer.

FF transmission electron microscopy

For the characterisation of the different phases by FF transmission electron microscopy (FF-TEM) a small amount of surfactant solution is placed on a 0.1-mm-thick copper plate and is covered with a second copper plate. This "sandwich" is frozen by plunging

it into liquid propane cooled by liquid nitrogen. The fracturing of the sample and the replication are carried out with a Biotech 2005 apparatus (Leybold–Heraeus) at a temperature of −100 °C. The Pt/C was deposited at an angle of 45°; the replicas were examined with a CEM 902 TE microscope (Zeiss).

Differential scanning calorimetry

The differential scanning calorimetry (DSC) measurements were carried out with a Setaram Micro-DSC apparatus. The temperature range was varied from 0 to 100 °C; the scanning rate for the samples was 0.2 °C min^{-1}.

Specific conductivity

For the specific conductivity measurements of the surfactant solutions a WTW 2000 conductometer with a platinum electrode (cell constant 0.1 cm^{-1}) was used.

Rheology

The rheological properties of the surfactant solutions were studied with a Paar OCR-D capillary viscometer for low viscosities and with a Bohlin rheometer for higher viscosities.

Small-angle neutron scattering

The small-angle neutron scattering (SANS) measurements were carried out with the V4 instrument of the Hahn–Meitner Institute in Berlin. The samples were prepared in D_2O and thermostated at 25 °C during the measurement. The variation of the wavelength of the neutrons used and the different distances between the sample and the detector of the scattered neutrons allow the measurement of the SANS spectra within a q-value region from 0.01 to 0.15 $Å^{-1}$.

Results and discussion

Phase diagram of $C_{12}C_{11}$DMABr

The binary water/surfactant phase diagrams for the C_xC_yDMABr surfactants listed in Table 1 were determined for temperatures between 15 and 70 °C. First, the phase behaviour of $C_{12}C_{11}$DMABr will be described in detail. Then the phase diagrams of the other systems will be described and differences which arise when the x and y values are varied will be discussed.

The temperature and concentration-dependent phase behaviour of $C_{12}C_{11}$DMABr in water is shown in Fig. 1. The cmc of the surfactant, determined by surface tension measurements [24], is 0.1 mM (9×10^{-3} wt%). With

Table 1 List of the *N*-alkyl-*N*-alkyl′-*N*,*N*-dimethylammonium bromide (C_xC_yDMABr) surfactants synthesised

	$C_{14}C_{10}$DMABr	
$C_{12}C_{11}$DMABr	$C_{14}C_{11}$DMABr	$C_{16}C_{11}$DMABr
	$C_{14}C_{12}$DMABr	$C_{16}C_{12}$DMABr
	$C_{14}C_{14}$DMABr	$C_{16}C_{14}$DMABr
		$C_{16}C_{16}$DMABr

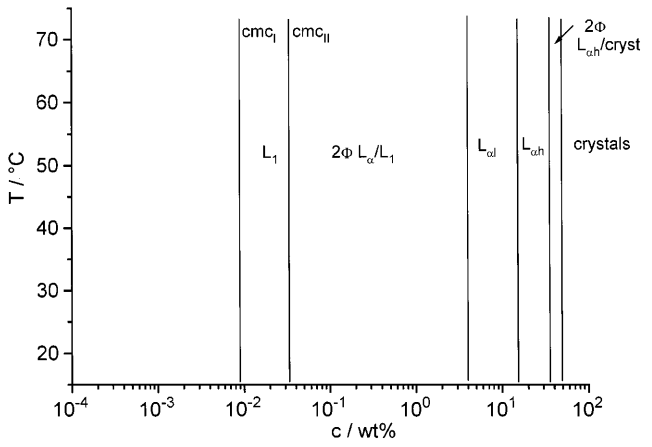

Fig. 1 The phase diagram of the $C_{12}C_{11}$DMABr-dimethylammonium bromide ($C_{12}C_{11}$DMABr) water binary system

increasing surfactant concentration, a second break (cmc_{II}) in the σ-log (c) curve is found at 0.7 mM (3.4×10^{-2} wt%) due to a change in micellar shape. The samples become more and more turbid with increasing surfactant concentration, still have water viscosity, do not separate into two phases and do not show any birefringence between crossed polarisers up to a concentration of 4 wt%. For surfactant concentrations above 4 wt% the solutions are still turbid, but highly viscous and show birefringence. The "Schlieren" texture of the birefringent samples is an indication of the presence of an $L_{\alpha 1}$ phase consisting of multilamellar vesicles. Samples of the $L_{\alpha 1}$ phase show a yield-stress value which rises with increasing surfactant concentration. Above 15 wt% of surfactant the texture of the birefringence between crossed polarisers changes from the "Schlieren" texture of the $L_{\alpha 1}$ phase to the domain-type structure of the classical $L_{\alpha h}$ phase that consists of stacked planar bilayers [26]. The samples are still slightly turbid, have a lower viscosity than samples of the $L_{\alpha 1}$ phase but have only a very small yield-stress value. For even higher surfactant concentrations ($c > 40$ wt%) a $L_{\alpha h}$/crystalline or L_1/crystalline two-phase region ($c > 60$ wt%) appears.

FF-TEM micrographs and DIC pictures for $C_{12}C_{11}$DMABr

To obtain further information on the aggregation behaviour of $C_{12}C_{11}$DMABr, microscopy techniques were used to characterise the aggregates formed in the different concentration regions in the phase diagram. The micellar solution above the cmc_{II} is followed by a nonseparated two-phase L_1/L_α region in which unilamellar vesicles are present. A FF-TEM micrograph of a 0.5 wt% solution of $C_{12}C_{11}$DMABr is shown in Fig. 2a. The unilamellar vesicles which are shown on the micrograph are polydisperse in size. The mean diameter

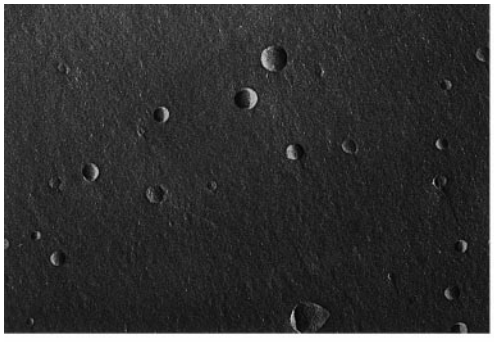

a 500nm

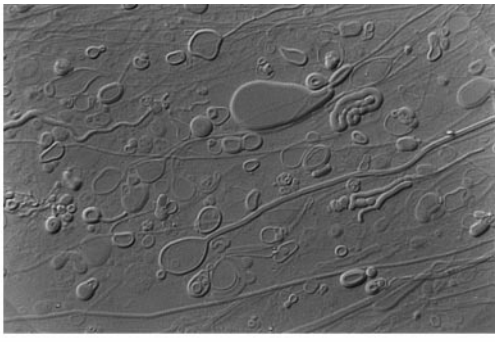

b 50µm

c 200nm

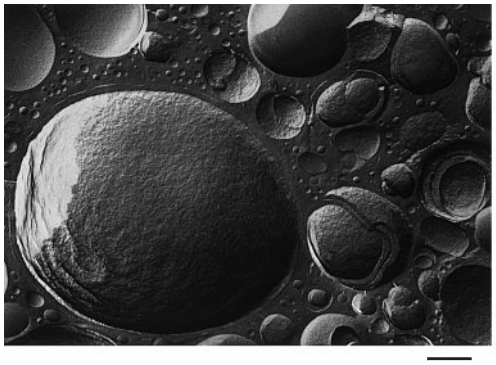

d 700nm

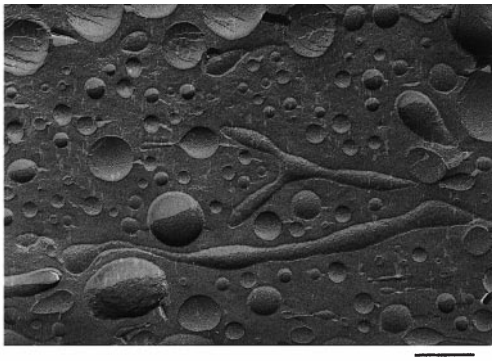

e 200nm

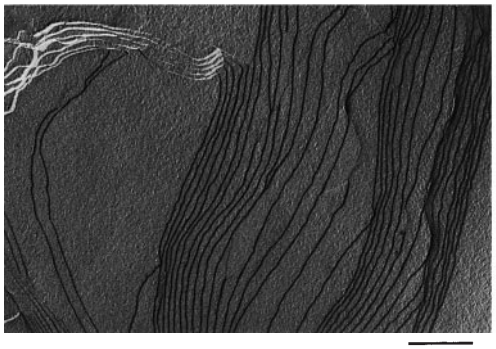

f 350nm

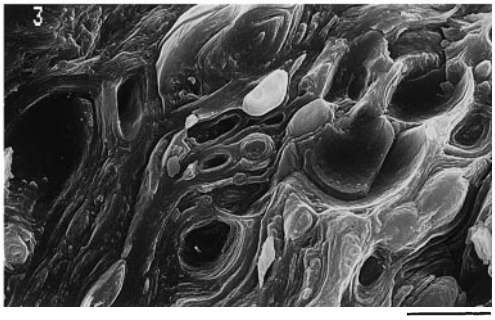

g 10µm

◄

Fig. 2a–g Freeze-fracture (*FF*) transmission electron microscope micrographs of the aggregates in aqueous solutions of $C_{12}C_{11}$ DMABr with various concentrations. **a** 0.5 wt% (DIC-micrograph); **b** 1 wt%; **c** 2 wt%; **d**, **e** 5 wt%; **f** 20 wt%; **g** 20 wt%, FF scanning electron microscope micrograph

of the vesicles that can be determined from the micrograph is about 125 ± 60 nm. The ratio of the area of the vesicles to the total area of the micrograph is around 4%. This value of 4% is consistent with the concentration of the surfactant in the sample, because the total volume of a vesicle [$(4/3)\ R^3\ \pi$] is about 10 times larger than the volume of surfactant in the shell of the vesicles ($4R^2\,\pi\,d$).

With increasing surfactant concentration within the two-phase region cylindrical aggregates, the so-called microtubuli, can be found in addition to the unilamellar vesicles. This can clearly be seen in the DIC micrograph of a 1 wt% solution in Fig. 2b and the FF-TEM picture of a 2 wt% solution in Fig. 2c. On the DIC picture some of the microtubuli seem to "grow" out of the vesicles, while some of them are not connected to a vesicle. It can also be seen that most of the microtubuli are totally stretched, while some of them are folded. The length of the tubuli on the DIC micrograph varies between 50 and 100 °C; the diameter of the cylindrical aggregates is about 150 nm. Some of the vesicles in the 1 wt% solution are no longer unilamellar but seem to have at least two or three bilayers. In addition to these uni- and oligolamellar vesicles big vesicles which have one or two smaller vesicles trapped inside can be seen on the DIC micrograph. The microtubuli in the FF-TEM picture of a 2 wt% solution are between 300 and 1000 nm long and their diameter lies between 50 and 100 nm. They are totally disconnected from the vesicles and are either straight or bent. The coexisting unilamellar vesicles are still polydisperse in their diameter, which is around 150 ± 80 nm; the volume fraction of the unilamellar vesicles and the microtubuli in the 2 wt% solution on the micrograph is around 9%. In contrast to the DIC picture of the 1 wt% solution, the FF-TEM micrograph does not show any oligolamellar vesicles. Only one of the vesicles shown seems to have two shells.

Above a surfactant concentration of 4 wt%, the L_1/L_α two-phase region is followed by the $L_{\alpha 1}$ one-phase region. The FF-TEM pictures of a 5 wt% solution of $C_{12}C_{11}$DMABr are shown in Fig. 2d and e. In Fig. 2d one can clearly see large multilamellar vesicles coexisting with small unilamellar vesicles. The size of the vesicles is still very polydisperse and can be determined to be between 70 and 150 nm for the unilamellar vesicles and between 500 nm and 5 μm for the large multilamellar vesicles. In Fig. 2d some of the multilamellar vesicles are cross fractured and the interlamellar spacing between the bilayers can be determined to be about 40–50 nm. For most of the large vesicles the fracture has followed the outermost shell and so only one layer can be seen. The packing of the vesicles in the micrograph is very dense. The unilamellar vesicles are mainly packed in-between the large multilamellar vesicles. The high viscosity and the yield-stress value of the solutions of the $L_{\alpha 1}$ phase can thus be explained [27–30]. In the FF-TEM micrograph in Fig. 2e cylindrical aggregates in the $L_{\alpha 1}$ phase can be seen in addition to vesicles. The two microtubuli in the picture lie between the vesicles, are 600 and 1300 nm long and have a diameter of about 60 nm. None of the vesicles shown in Fig. 2e show a break through the different bilayers of the multilamellar vesicles; thus the interlamellar spacing cannot be determined. This indicates that the surfactant bilayers seem to have a few defects, because defects are normally responsible for a cross-fracture of the multilamellar vesicles. The size distribution of the vesicles is still polydisperse with diameters between 50 and 400 nm.

For concentrations above 15 wt% the single-phase $L_{\alpha 1}$region turns into the single-phase $L_{\alpha h}$ region. The FF-TEM micrograph of a 20 wt% solution of $C_{12}C_{11}$DMABr shows the typical steps that can be found for planar bilayers (Fig. 2f). From the distance between the different steps the mean lamellar distance within the planar bilayers can be determined to be 15–20 nm. Studying the 20 wt% solution with the FF-SEM method (Fig. 2g), one can find that this solution does not only consist of planar bilayers but also includes very large multilamellar vesicles with a diameter of several microns. These vesicles and the planar bilayers are responsible for the relatively high viscosity and the still-existent yield-stress value of the $L_{\alpha h}$ phase of $C_{12}C_{11}$DMABr.

The C_xC_yDMABr phase diagram

The phase diagrams for the other C_xC_yDMABr systems are shown in Fig. 3. All the C_xC_yDMABr surfactants do not change the aggregation form when the temperature is changed. Also the only liquid-crystalline phase found for all the surfactants is the lamellar phase and the phase sequence L_1-L_1/L_α-$L_{\alpha 1}$-$L_{\alpha h}$ is still the same for all homologues.

The largest difference in the phase behaviour with regard to the chain lengths x and y is the existence of the cylindrical tubuli. They were only found for the systems $C_{12}C_{11}$DMABr, $C_{14}C_{10}$DMABr, $C_{14}C_{11}$DMABr and $C_{14}C_{12}$DMABr. The surfactants of the $C_{16}C_y$DMABr homologous series and the symmetrical surfactant $C_{14}C_{14}$DMABr did not show this aggregation form within the whole concentration range.

The coexistence of vesicles and microtubuli indicates that the surfactant molecules are able to build structures with different spontaneous curvatures for the same solution. While the surfactant molecules in the vesicles

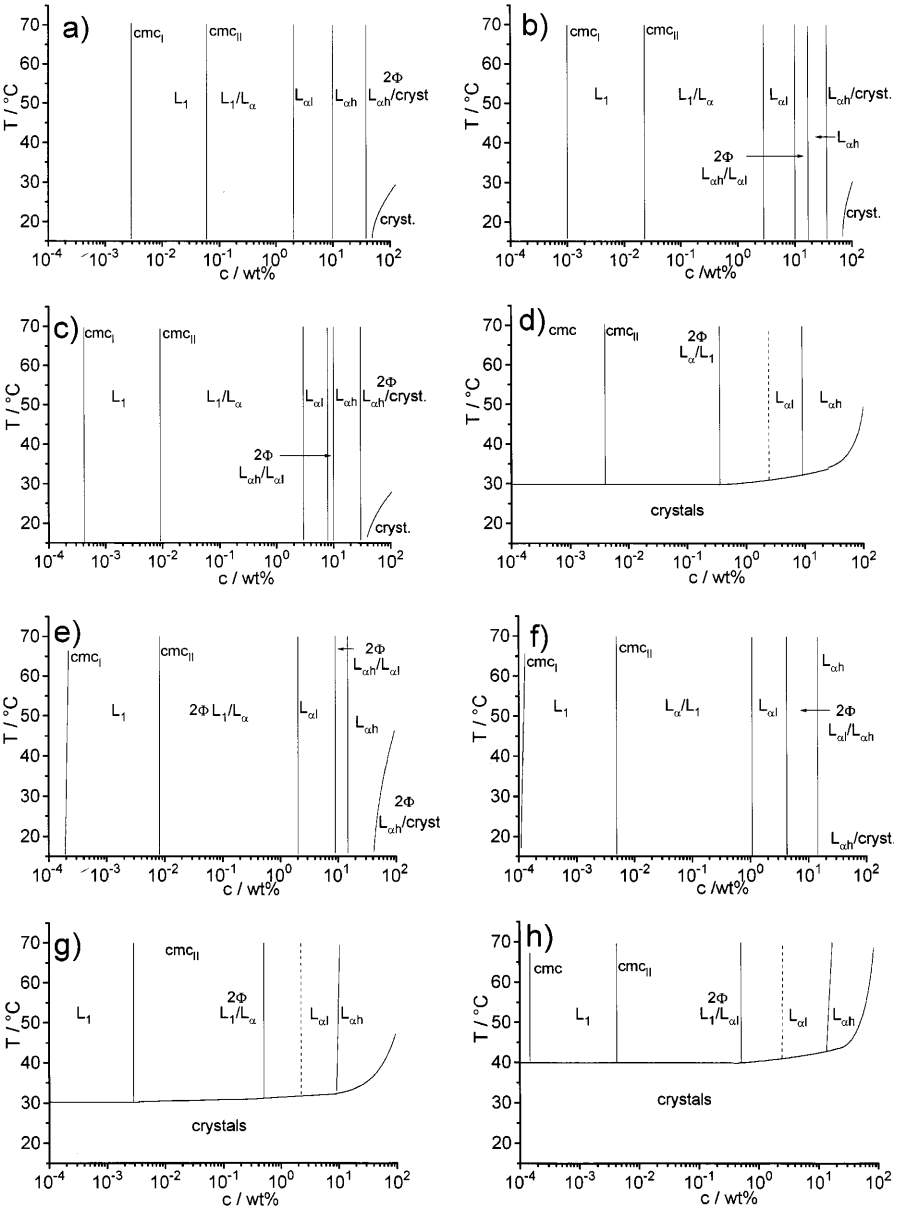

Fig. 3a–h Phase diagrams of the C_xC_yDMABr/water binary systems: **a** $x = 14$, $y = 10$; **b** $x = 14$, $y = 11$; **c** $x = 14$, $y = 12$; **d** $x = 14$, $y = 14$; **e** $x = 16$, $y = 11$; **f** $x = 16$, $y = 12$; **g** $x = 16$, $y = 14$; **h** $x = 16$, $y = 16$

have two curvatures which are the same but depend on the diameter of the aggregate, the surfactant molecules in the microtubuli with their large, almost planar, regions have two very different curvatures. It seems that the surfactants of the $C_{16}C_y$DMABr homologous series and the symmetrical surfactant $C_{14}C_{14}$DMABr are not able to adjust these different spontaneous curvatures within one and the same solution and therefore they do not form microtubuli in addition to vesicles.

The $L_{\alpha 1}/L_{\alpha h}$ two-phase region

The samples $C_{14}C_{11}$DMABr, $C_{14}C_{12}$DMABr, $C_{16}C_{11}$DMABr and $C_{16}C_{12}$DMABr form a $L_{\alpha 1}/L_{\alpha h}$ two-phase region between the $L_{\alpha 1}$ and $L_{\alpha h}$ single-phase regions with macroscopically separated phases. This can be seen for the four samples of $C_{16}C_{12}$DMABr with 7, 8, 9 and 10 wt% between crossed polarisers in Fig. 4. The upper phase shows the texture with the domain-type structure that characterises the $L_{\alpha h}$ phase while the "Schlieren" texture at the bottom of the test tube is typical for the $L_{\alpha 1}$ phase [26]. The two phases are also different in their flow properties: while the upper phase flows when the sample is tilted, the $L_{\alpha 1}$ phase stays at the bottom because of its yield stress. The surfactant concentration in the two macroscopically separated phases can be determined by density measurements: the density decreases linearly with increasing surfactant concentration. For the $L_{\alpha 1}$ phases at the bottom of the

test tube, a surfactant concentration of around 5 wt% can be determined for all solutions, while the surfactant concentration in the $L_{\alpha h}$ phases at the top of the test tubes is found to be around 17.5 wt%. This more or less constant surfactant content in the $L_{\alpha 1}$ and $L_{\alpha h}$ phases also explains the increasing phase volumes of the $L_{\alpha h}$ phase in this two-phase region with increasing surfactant concentration.

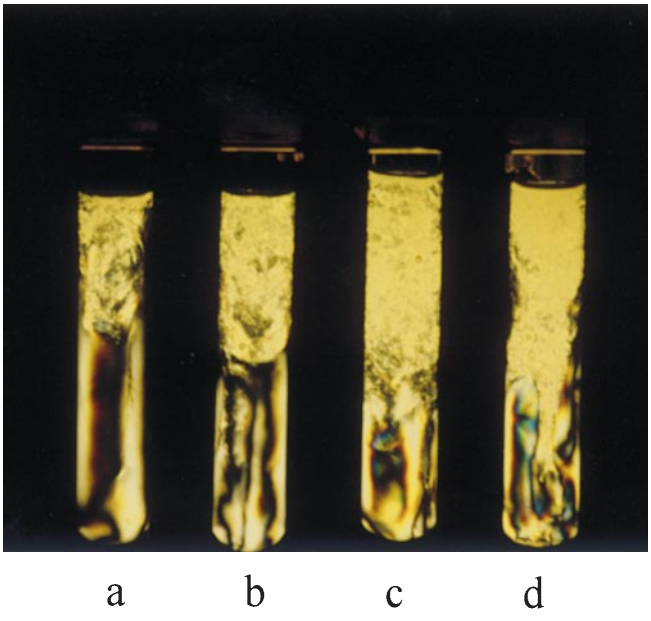

Fig. 4 Photographs of the $L_{\alpha h}/L_{\alpha 1}$ two-phase region in the $C_{16}C_{12}$DMABr/water binary system with various concentrations (*a*: 7 wt%; *b*: 8 wt%; *c*: 9 wt%; *d*: 10 wt%) at 25 °C between crossed polarisers (on the *top* the domain-like texture of the $L_{\alpha h}$ phase, on the *bottom* the Schlieren texture of the $L_{\alpha 1}$ phase)

Iridescent phases

For the three homologues with the largest x and y values ($C_{14}C_{14}$DMABr, $C_{16}C_{14}$DMABr and $C_{16}C_{16}$DMABr) phases with iridescent colours are found in the $L_{\alpha 1}$ one-phase region for surfactant concentrations between 0.6 and 2.5 wt%. The colour of the samples changes with increasing surfactant concentration from red to green, blue-green and finally blue. This can be seen in Fig. 5 for samples of $C_{14}C_{14}$DMABr with 1.0, 1.2, 1.4 and 1.6 wt% at 35 °C.

DSC measurements

While for $C_{12}C_{11}$DMABr no Krafft point could be found by DSC measurements even for samples with high surfactant concentrations, some other homologues clearly had a Krafft temperature. The DSC measurement of a 10 wt% solution of the surfactant $C_{14}C_{14}$DMABr with the curves for heating and cooling is shown in Fig. 6. The maxima and minima for the two curves do not occur at the same temperature but the maximum of the curve obtained by cooling the sample is shifted to a lower temperature. This behaviour was found for all C_xC_yDMABr homologues and is due to a kinetic hindrance of the crystallisation of the surfactant. The solutions of all surfactants can be undercooled and metastable phases can be obtained. This undercooling

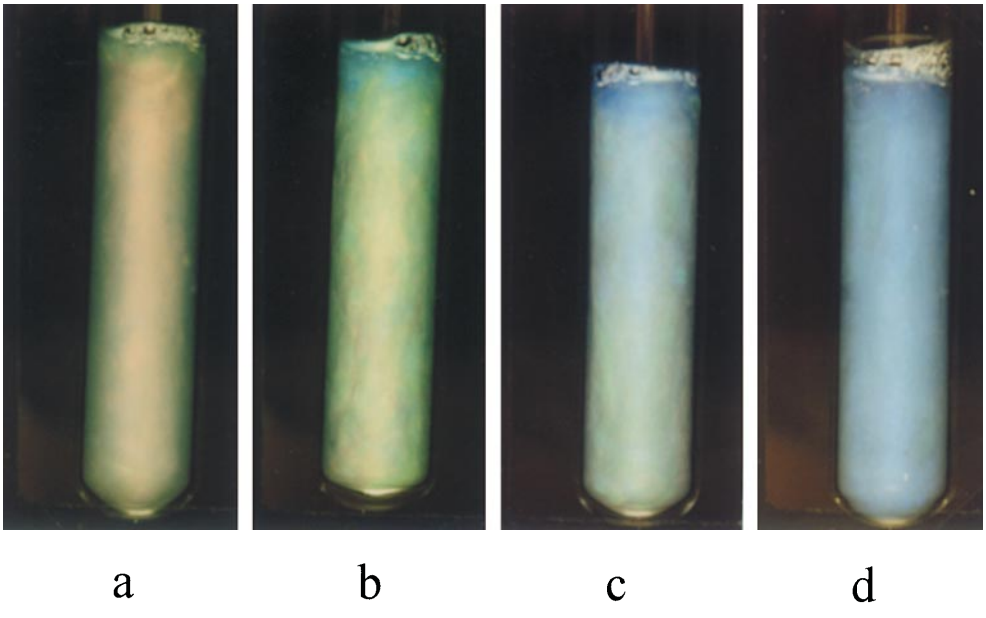

Fig. 5 Photographs of solutions with iridescent colours in the $C_{14}C_{14}$DMABr/water binary system with various concentrations (*a*: 1.0 wt%; *b*: 1.2 wt%; *c*: 1.4 wt%; *d*: 1.6 wt%) at 35 °C

may also be the reason why the surfactants $C_{12}C_{11}$DMABr, $C_{14}C_{10}$DMABr and $C_{14}C_{11}$DMABr, whose Krafft points are even lower than that of $C_{14}C_{12}$DMABr, could not be studied with the DSC method. The heat of melting, that can be determined from the area below the DSC peaks, is nearly the same for all surfactants and is between 26 and 28 mJ/mg surfactant. In Table 2 all Krafft points determined as the maximum temperature of the DSC peak from heating are listed.

SANS measurements

To get some information on the thickness of the lamellae in the unilamellar vesicles and the interlamellar spacing in the $L_{\alpha 1}$ and $L_{\alpha h}$ phases SANS measurements were carried out for all homologues for surfactant concentrations of 10 mM and 20 wt%. Furthermore, concentration series through the $L_{\alpha 1}$ and $L_{\alpha h}$ one-phase regions were carried out for the three C_xC_{11}DMABr surfactants. A typical $I(q)/q$ plot for the surfactant $C_{12}C_{11}$DMABr at 10 mM and 20 wt% surfactant is shown in Fig. 7. The interlamellar spacing in the highly concentrated solutions can be determined from the q value, q_{max}, of the maximum in the $I(q)/q$ plot using Eq. (1) where n and D represent the number of the peak maximum and the interlamellar spacing, respectively.

$$q_{max} = n\frac{2\pi}{D} \quad . \tag{1}$$

With the knowledge of the interlamellar spacing, D, the thickness, d, of the bilayer can be determined from the volume fraction Φ using Eq. (2)

$$\Phi = \frac{d}{D} \quad . \tag{2}$$

A second possibility to determine the thickness of the bilayer is the so-called Kratky–Porod plot. For this, the logarithm of $I(q)\,q^2$ is plotted against q^2 and the slope of the linear regression corresponds to $-d^2/12$. The Kratky–Porod plot for the scattering curve of a 10 mM solution of $C_{12}C_{11}$DMABr is shown in Fig. 8. Table 3 contains all d values for the surfactants investigated at concentrations of 10 mM and 20 wt%,

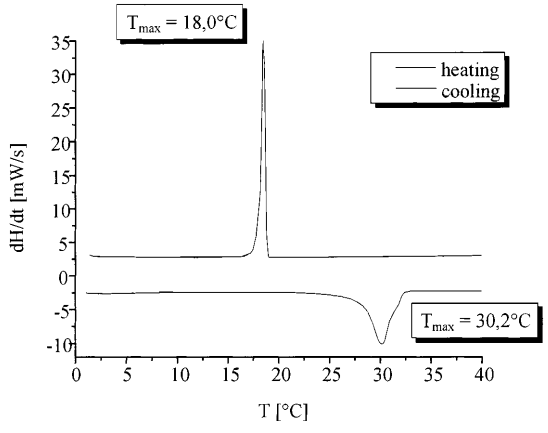

Fig. 6 Differential scanning colorimetry curves for a 10 wt% solution of $C_{14}C_{14}$DMABr in water

Table 2 Krafft points of homologous C_xC_yDMABr surfactants determined from differential scanning calorimetry measurements

Surfactant	Kraff point (°C)
$C_{14}C_{12}$DMABr	17.5
$C_{14}C_{14}$DMABr	30.2
$C_{16}C_{11}$DMABr	19.3
$C_{16}C_{12}$DMABr	25.5
$C_{16}C_{14}$DMABr	33.0
$C_{16}C_{16}$DMABr	42.1

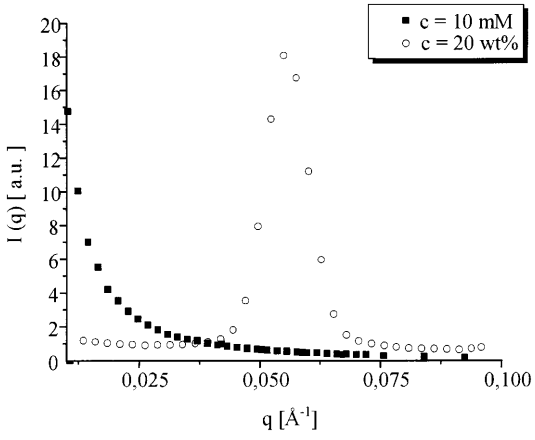

Fig. 7 The scattered intensity I of a neutron beam in aqueous solutions of $C_{12}C_{11}$DMABr with different concentrations as a function of the scattering vector q at 25 °C

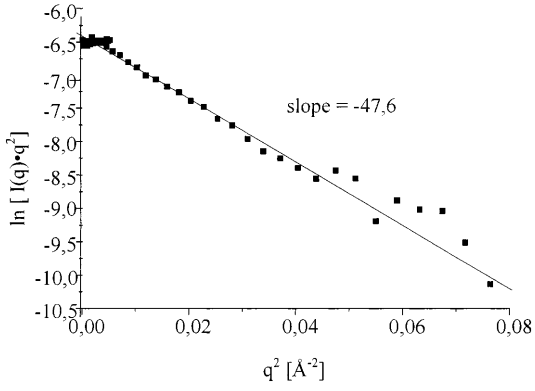

Fig. 8 The Kratky–Porod plot of small-angle neutron scattering measurements for a 10 mM aqueous solution of $C_{12}C_{11}$DMABr at 25 °C

respectively. The values for the 10 mM solutions are obtained by the Kratky–Porod method, while the values for the 20 wt% solutions are calculated from Eq. (2); the table shows that both values are in good agreement. Two facts are obvious from the results of the SANS measurements for the homologous surfactants: the thickness of the lamellae is dependent on both chain lengths x and y and the bilayers at 20 wt% are always slightly thinner than at 10 mM, but this difference is within the experimental error. However, if the experimental values of the bilayer thickness are compared with the theoretical length of the two alkyl chains according to Tanford's law [25], one finds that the thickness of the bilayers is generally smaller than the length of the alkyl chains. This might be due to some kind of folding of the alkyl chains in the bilayers or the surfactant molecules arrange themselves in the bilayer by tilting out of the plane. Further measurements must be done to explain the experimental data unambiguously.

The scattering curves for several concentrations of $C_{12}C_{11}$DMABr are shown in Fig. 9. The maximum in the $I(q)/q$ plot moves to higher q values for higher surfactant concentrations due to lower interlamellar spacing. The values of D with respect to the surfactant concentration for the three surfactants investigated are listed in Table 4. The plot of the experimental data of the interlamellar spacing D as a function of $1/\Phi$ in Fig. 10 for $C_{12}C_{11}$DMABr can be fitted very well with a linear regression, and so the lamellar thickness d is given by the slope of the line. This also means that the bilayer thickness remains constant over the whole concentration range of the $L_{\alpha 1}$ and $L_{\alpha h}$ phases. In the case of $C_{12}C_{11}$DMABr the thickness of the lamellae in the $L_{\alpha 1}$ and $L_{\alpha h}$ phases is 22.1 Å. The same plot of D against $1/\Phi$ can be carried out for the other surfactants, $C_{14}C_{11}$DMABr and $C_{16}C_{11}$DMABr, and yields 25.8 Å and 28.7 Å, respectively, as the thickness of the bilayers.

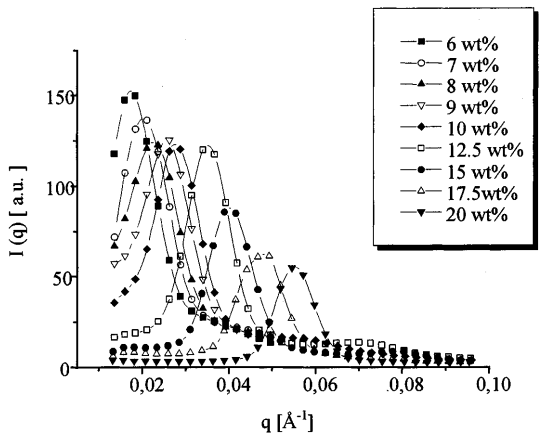

Fig. 9 The scattered intensity I of a neutron beam in aqueous solutions of $C_{12}C_{11}$DMABr with various concentrations at 25 °C

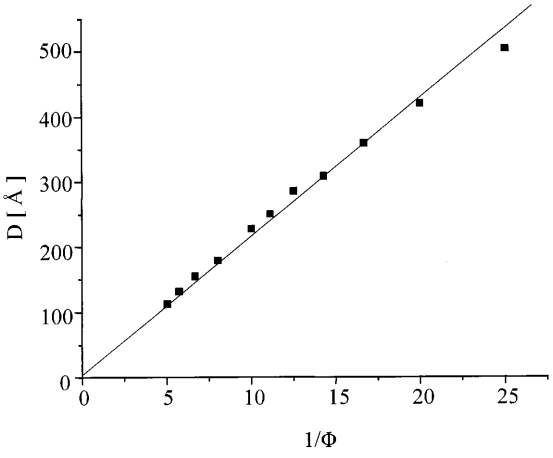

Fig. 10 The interlamellar spacing D for aqueous solutions of $C_{12}C_{11}$DMABr as a function of the volume fraction Φ at 25 °C

Table 3 Values of the thickness of the bilayers with respect to the chain lengths x and y for unilamellar vesicles at 10 mM and planar bilayers at 20 wt% surfactant concentration determined from small-angle neutron scattering (*SANS*) measurements at 25 °C

Surfactant	d (Å) (c = 10 mM)	d (Å) (c = 20 wt%)
$C_{12}C_{11}$DMABr	23.9	22.6
$C_{14}C_8$DMABr	–	21.9
$C_{14}C_9$DMABr	23.7	22.3
$C_{14}C_{10}$DMABr	24.4	23.1
$C_{14}C_{11}$DMABr	25.7	23.7
$C_{14}C_{12}$DMABr	27.2	24.5
$C_{16}C_8$DMABr	–	23.2
$C_{16}C_9$DMABr	25.1	24.0
$C_{16}C_{10}$DMABr	26.3	24.7
$C_{16}C_{11}$DMABr	27.6	25.8
$C_{16}C_{12}$DMABr	28.5	26.8

Table 4 Interlamellar spacing D with respect to surfactant concentration for the three C_xC_{11}DMABr homologues with x = 12, 14 and 16 from SANS measurements at 25 °C

c (wt%)	$C_{12}C_{11}$DMABr	$C_{14}C_{11}$DMABr	$C_{16}C_{11}$DMABr
4	502.7 Å	592.8 Å	622.1 Å
5	418.9 Å	487.1 Å	–
6	359 Å	418.9 Å	–
7	308 Å	353.0 Å	371.8 Å
8	285.6 Å	303.5 Å	–
9	250.3 Å	–	281.8 Å
10	227.7 Å	233.6 Å	250.5 Å
12.5	179.0 Å	183.2 Å	201.9 Å
15	154.8 Å	160.3 Å	167.0 Å
17.5	132.0 Å	138.4 Å	144.7 Å
20	113.2 Å	118.6 Å	128.7 Å

Conductivity measurements

Conductivity measurements over the whole concentration range from 1×10^{-3} to 20 wt% were carried out for all the surfactants. A plot of κ versus $\log c$ for $C_{12}C_{11}$DMABr is shown in Fig. 11; this plot is typical for all homologous C_xC_yDMABr surfactants. For low surfactant concentrations two breaks in the $\kappa/\log c$ plot can be found at surfactant concentrations of 8×10^{-3} wt and 4×10^{-2} wt%. These values agree very well with the cmc and cmc_{II} values determined from surface tension measurements. Above the cmc_{II}, the κ value initially remains more or less constant with increasing surfactant concentration. This is probably due to the increase in the concentration of the unilamellar vesicles in which some of the counterions are entrapped and can no longer contribute to the conductivity. Above about 1 wt% surfactant concentration, the κ values start to rise again until the $L_{\alpha 1}$ one-phase region is reached. This rise in conductivity may be due to an increase in the number density of the unilamellar vesicles instead of a growth of the vesicles with increasing surfactant concentration which would lead to more free counterions and hence to higher conductivities. This effect was also seen in the FF-TEM pictures, where the mean radius of the vesicles did not increase with the surfactant concentration but remained constant over the whole L_1/L_α region. Above 4 wt% surfactant concentration, the boundary of the $L_{\alpha 1}$ phase, the κ values remain constant up to 20 wt%. No decrease in the conductivity was found at the transition of the $L_{\alpha 1}$ phase to the $L_{\alpha h}$ phase. This effect could be explained with the large multilamellar vesicles that are still present in these solutions and lead to a higher conductivity than expected for a real classical $L_{\alpha h}$ phase with planar bilayers. The corresponding plots for all homologous surfactants have the same shape; the only difference is the absolute value of the conductivity because with increasing chain lengths x and y the conductivity decreases for equivalent surfactant concentrations.

Rheological measurements

Rheological measurements were carried out for all surfactants over a wide concentration range from above the cmc to 20 wt%. The typical concentration-dependent viscosity behaviour for $C_{12}C_{11}$DMABr for concentrations between the cmc and the phase boundary of the $L_1/L_{\alpha 1}$ phases is shown in Fig. 12. This behaviour is also typical for all other systems. The viscosity remains close to the water viscosity up to concentrations of about 0.4 wt%. Above this concentration, the increasing number of unilamellar vesicles in the solutions leads to an increase in the η_0 values, which are higher than 100 mPa s for the 3 wt% solution.

When entering the $L_{\alpha 1}$ phase, the η_0 values can no longer be determined because the solutions show the typical rheological behaviour of viscoelastic surfactant solutions with a yield-stress value. A frequency-dependent rheogram of a 10 wt% solution of $C_{12}C_{11}$DMABr is shown in Fig. 13: the complex viscosity $|\eta^*|$ decreases linearly with increasing frequency and the values of the moduli G' and G'' are constant over the whole frequency region with $G' \gg G''$. The values of $|\eta^*|$ and G' at a constant frequency of 1 Hz increase with surfactant concentration within the $L_{\alpha 1}$ phase and are more or less constant in the $L_{\alpha h}$ phase. This behaviour is due to the existence of large multilamellar vesicles in addition to the planar bilayers as seen in the FF-SEM micrographs of a 20 wt% solution of $C_{12}C_{11}$DMABr. This behaviour is shown in Fig. 14 for $C_{12}C_{11}$DMABr. The concentration-dependent rheological behaviour of all other surfactants of the C_xC_yDMABr homologous series is the same as shown for $C_{12}C_{11}$DMABr except that with increasing chain lengths the values of $|\eta^*|$, G' and G'' are

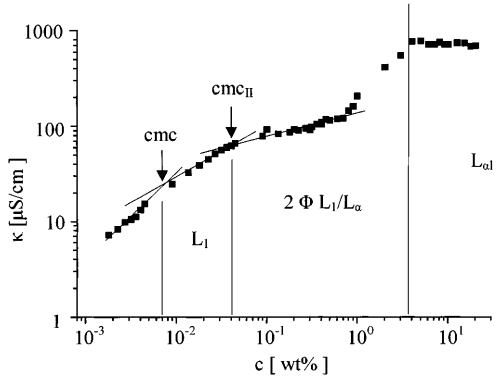

Fig. 11 The electric conductivity κ of aqueous solutions of $C_{12}C_{11}$DMABr as a function of the logarithm of the concentrations c at 25 °C

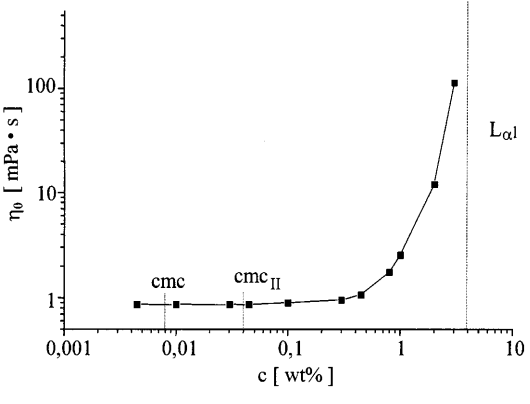

Fig. 12 The zero-shear viscosity η_0 for the L_1 phase in the $C_{12}C_{11}$DMABr/water binary system as a function of the concentration c at 25 °C

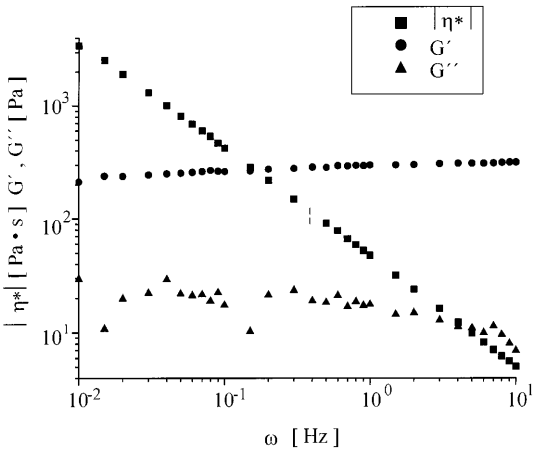

Fig. 13 The storage modulus G', the loss modulus G'' and the complex viscosity $|\eta^*|$ for a 10 wt% aqueous solution of $C_{12}C_{11}$DMABr as a function of the oscillation frequency ω at 25 °C

lower for samples with the same surfactant concentration.

In addition to $|\eta^*|$, G' and G'' the yield stress value σ_y of the viscoelastic surfactant solutions was determined. A typical plot of the shear stress σ against the shear rate for a 5 wt% solution of $C_{12}C_{11}$DMABr is shown in Fig. 15. The yield-stress value is determined to be the shear-stress value when the solution starts to flow, i.e. when the shear rate begins to increase from 0 s^{-1}. The concentration-dependent yield-stress value for $C_{12}C_{11}$DMABr is shown in Fig. 16. Again the value increases within the $L_{\alpha 1}$ phase with increasing surfactant concentration and does not drop to zero immediately when entering the $L_{\alpha h}$ phase. This means that first of all the packing of the multilamellar vesicles gets stronger within the $L_{\alpha 1}$ phase and that the existence of the multilamellar vesicles in the $L_{\alpha h}$ phase leads to a low yield stress in these solutions. The yield stress shows the

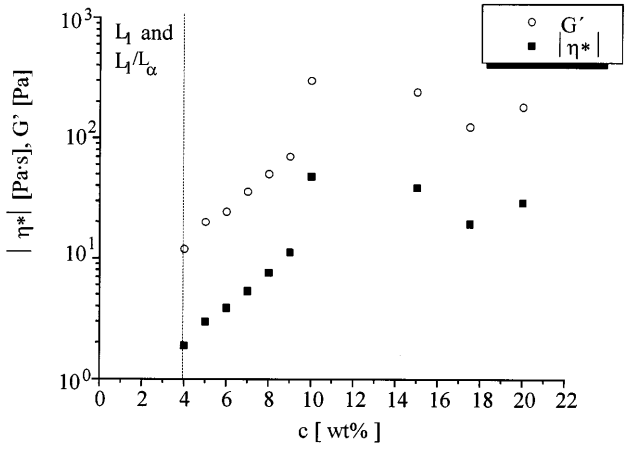

Fig. 14 The complex viscosity $|\eta^*|$ and the storage modulus G′ at an oscillation frequency of 1 Hz for aqueous solutions of $C_{12}C_{11}$DMABr as a function of the concentration c at 25 °C

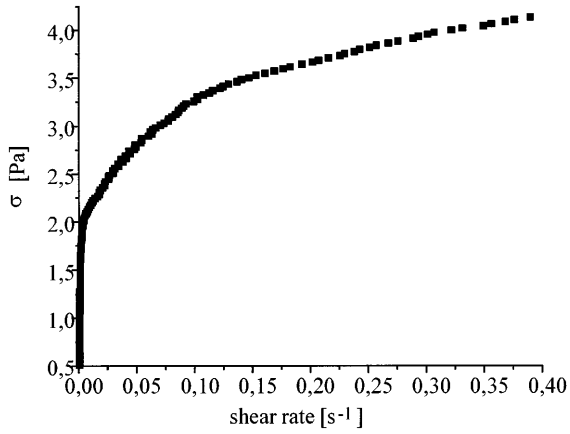

Fig. 15 The stress σ for a 5 wt% aqueous solution of $C_{12}C_{11}$DMABr as a function of the shear rate at 25 °C

same dependence on the chain lengths as the viscosity and the moduli: with increasing chain lengths the values decrease for equivalent surfactant concentrations.

Conclusions

All the homologues of the C_xC_yDMABr surfactants show an athermal phase behaviour and form only lamellar liquid-crystalline phases with a great variety in morphologies, i.e. unilamellar and multilamellar vesicles, microtubuli and planar bilayers. Some homologues form solutions with iridescent colours and for some surfactants a macroscopically separated $L_{\alpha 1}/L_{\alpha h}$ two-phase region can be found.

SANS measurements showed that the thickness of the bilayers, either in unilamellar vesicles or planar bilayers, is dependent on both alkyl chain lengths x and y and is lower than the theoretically expected value. The interlamellar distances in the $L_{\alpha 1}$ and the $L_{\alpha h}$ phases show

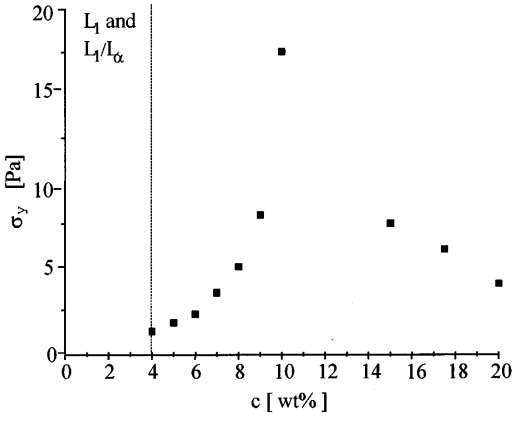

Fig. 16 The yield stress value σ_y for aqueous solutions of $C_{12}C_{11}$DMABr as a function of the concentrations c at 25 °C

a linear dependence on the volume fraction of the surfactant.

Conductivity and viscosity measurements for all the surfactants are in good agreement with the observed phase behaviour and are also dependent on both chain lengths.

Acknowledgements Financial support of this work by the Deutsche Forschungsgemeinschaft (DFG) and the Fonds der Chemischen Industrie and further support by the donation of the alkyldimethylamines by Hoechst-Gendorf are gratefully acknowledged.

References

1. Bansal VK, Shah DO (1978) J Colloid Interface Sci 65:451
2. Hoffmann H (1992) Surf Sci Ser 144:169
3. Kahlweit M, Strey R, Busse G (1990) J Phys Chem 94:3881
4. Hoffmann H, Munkert U, Thunig C, Valiente M (1994) J Colloid Interface Sci 163:217
5. Jönsson B, Wennerström H (1987) J Phys Chem 91:378
6. Anderson D, Wennerström H, Olsson U (1989) J Phys Chem 93:4243
7. Porte G, Appell J, Bassereau P, Marignan J (1989) J Phys (Paris) 50:1335
8. Gazeau D, Bellocq AM, Roux D, Zemb T (1989) Europhys Lett 9:447
9. Strey R, John W, Porte G, Bassereau P (1990) Langmuir 6:1635
10. Miller CA, Ghosh O, Benton W (1986) Colloids Surf 19:197
11. Israelachvili JN, Mitchell DJ, Ninham BW (1976) J Chem Soc Faraday Trans II 72:1525
12. Munkert U, Hoffmann H, Thunig C, Meyer HW, Richter W (1993) Prog Colloid Polym Sci 93:137
13. Strey R, Schomäcker R, Roux D, Nallet F, Olsson U (1990) J Chem Soc Faraday Trans. 86:2253
14. Gomati R, Appell J, Bassereau P, Marignan J, Porte G (1987) J Phys Chem 91:6203
15. Okamura H, Imae T, Takagi K, Sawaki Y, Furusaka M (1996) J Colloid Interface Sci 180:98
16. Jönsson B, Wennerström H (1987) J Phys Chem 91:338
17. Hertel G, Hoffmann H (1988) Prog Colloid Polym Sci 76:123
18. Hertel G, Hoffmann H (1989) Liq Cryst 5:1883
19. Hertel G (1989) PhD thesis. University of Bayreuth
20. Kunieda H, Shinoda K (1978) J Phys Chem 82:1710
21. Dubois M, Zemb T (1991) Langmuir 7:1352
22. Dubois M, Gulik-Krzywicki T, Cabane B (1993) Langmuir 9:673
23. Ricoul F, Dubois M, Zemb T (1997) J Phys II 7:69
24. Haas S, Hoffmann H (1996) Prog Colloid Interface Sci 101:131
25. Tanford C (1973) The hydrophobic effect. Wiley, New York
26. Bergmeier M, Gradzielski M, Hoffmann H, Mortensen K (1999) J Phys Chem B 103:1605
27. Thunig C, Platz G, Hoffmann H (1992) Springer Proc Phys 66:266
28. Hoffmann H (1994) ACS Symp Ser 578:1
29. Hoffmann H, Thunig C, Schmiedel P, Munkert U, Ulbricht W (1994) Tenside Surfactants De 31:389
30. Hoffmann H, Thunig C, Schmiedel P, Munkert U (1995) Faraday Discuss 101:319